Functional connectivity favors aberrant visual network c-Fos expression accompanied by cortical synapse loss in amyloidosis.

Oliver J. L'Esperance, Josh McGhee, Garett Davidson, Adam Smith, Suraj Niraula, Jaichandar Subramanian*

Department of Pharmacology and Toxicology, School of Pharmacy, University of Kansas, Lawrence, KS 66045, USA

Running title: Functional and synaptic connectivity in amyloidosis

* Corresponding author address: Department of Pharmacology and Toxicology, 1251 Wescoe Hall Drive, Malott Hall Room 5060, University of Kansas, Lawrence, KS 66045

Phone: 785-864-3110; Email: jaichandar@ku.edu

Abstract

While Alzheimer's disease (AD) has been extensively studied with a focus on cognitive networks, sensory network dysfunction has received comparatively less attention despite compelling evidence of its significance in both Alzheimer's disease patients and mouse models. We recently found that neurons in the primary visual cortex of an amyloid mouse model exhibit an imbalance of postsynaptic structures favoring neuronal hyperactivity alongside increased c-Fos expression, which regulates plasticity and memory. Here, we map c-Fos expression in the visual network and across the brain in a mouse model of Alzheimer's disease. We found that the mouse model of AD exhibits aberrant c-Fos expression in multiple brain regions, and functional connectivity between brain regions is a significant predictor for aberrant cFos expression. We also show that depriving visual experience increases c-Fos expression in nonpathological controls across the brain but not the AD model, indicating experience-dependent plasticity deficits in multiple brain regions. Using in vivo and ex vivo imaging of presynaptic terminals, we found that aberrant cFos is associated with selective loss of excitatory cortical but not inhibitory or subcortical synapses. Our findings reveal novel structural and functional connectivity deficits in the visual network in amyloid pathology.

Introduction

Accumulating evidence underscores the coincidence of amyloid accumulation with cellular and synaptic loss within the visual cortex in individuals affected by Alzheimer's disease (AD) (Armstrong, 2009; Beach, Walker and McGeer, 1989; Cui et al., 2007; Frisoni et al., 2009; Hill et al., 2014; Hof and Morrison, 1990; Hwang et al., 2021; Ikonomovic et al., 2005; Jorge et al., 2020; Kurucu et al., 2022; Leuba and Kraftsik, 1994; Lewis et al., 1987; Mavroudis et al., 2011; Metsaars et al., 2003; Morrison, Hof and Bouras, 1991). AD patients exhibit visual impairments in contrast sensitivity, depth perception, and facial recognition (Cormack, Tovee and Ballard, 2000; Kirby, Bandelow and Hogervorst, 2010; Kusne et al., 2017; Mandal, Joshi and Saharan, 2012; Murphy, 2019; Zhang et al., 2023). In some patients, visual system disruption and visuospatial deficits emerge early in the disease progression, particularly in those developing the posterior cortical atrophy variant of AD (Best, Chapleau and Rabinovici, 2023; Chen et al., 2019; Crutch et al., 2012; Holden, Bettcher and Pelak, 2020; Maia da Silva et al., 2017; North et al., 2021; Yerstein et al., 2021). In these patients, cortical areas of the visual system frequently display irregular patterns of activation and functional connectivity (Gour et al., 2014; Hao et al., 2005; Wang et al., 2007). Mouse models of AD have also shown structural and functional visual system disruption (Chen et al., 2022; Chiquita et al., 2019; Criscuolo et al., 2018; Crowe and Ellis-Davies, 2014; Grienberger et al., 2012; Korzhova et al., 2021; Liebscher et al., 2016; Maya-Vetencourt et al., 2014; Niraula et al., 2023; Niraula, Yan and Subramanian, 2023; Papanikolaou et al., 2022; Rosales Jubal et al., 2021; Rudinskiy et al., 2012; van Veluw et al., 2020; William et al., 2012; William et al., 2021). Consistently, we also observed an increase in the expression of the immediate early gene c-Fos in the primary visual cortex of an amyloid mouse model (Niraula et al., 2023).

c-Fos is rapidly and transiently expressed following membrane depolarization and calcium influx in some neurons (Barth, Gerkin and Dean, 2004; Kawashima, Okuno and Bito, 2014; Mahringer et al., 2022; Morgan et al., 1987; Yap and Greenberg, 2018; Zangenehpour and Chaudhuri, 2002). Its low baseline expression, widespread expression profile, and close associations with learning and memory recall have made c-Fos$^+$ cell labeling an attractive tool for mapping and manipulating experience and memory associated neuronal ensembles (Barth, Gerkin and Dean, 2004; Guenthner et al., 2013; Liu et al., 2012; Reijmers et al., 2007). c-Fos$^+$ neurons fire more frequently and are more likely to share direct and indirect connections than c-Fos$^-$ neurons (Yassin et al., 2010). Due to these properties, correlated c-Fos expression between brain regions has frequently been used to represent functionally connected networks in a variety of contexts (Borcuk et al., 2022; Silva, Burns and Graff, 2019; Tanimizu et al., 2017; Teles et al., 2015; Vetere et al., 2017; Wheeler et al., 2013). Our recent observations of elevated visual cortical c-Fos expression, pro-excitatory shifts in postsynaptic structures, and impaired visual memory in an amyloid mouse model are suggestive of a structurally and functionally impaired visual network.

Here, we used a pre-plaque (5-6-months-old) mouse model of AD (J20 line (hAPP mice)) (Mucke et al., 2000) with human-like cortical amyloid deposition (Whitesell et al., 2019) to test how amyloid pathology disrupts visual network connectivity and whether functional connectivity contributes to aberrant c-Fos expression patterns. We also investigated the structural changes to excitatory and inhibitory presynaptic boutons in the visual network (primary visual cortex and dorsal lateral geniculate nucleus). We found that c-Fos$^+$ cell density is selectively increased in cortical regions of the visual network of hAPP mice, which showed strengthened functional interconnectivity. Furthermore, a region's functional connectivity strength across networks under

nonpathological conditions predicts its regional shifts in c-Fos$^+$ cell density in hAPP mice. Surprisingly, depriving visual experience increased c-Fos$^+$ cell density in the visual network of nonpathological (wild type (WT)) mice but not hAPP mice. In addition to functional disruptions of the visual network, we found structural evidence of subtype-specific loss of excitatory presynaptic termini in the visual cortex but not in the subcortical lateral geniculate nucleus. However, short-term bouton dynamics were unchanged in hAPP mice.

Results

Aberrant c-Fos$^+$ cell distribution emerges in cortical regions of the visual network in hAPP mice.

Using *in vivo* calcium transient imaging in awake mice, we recently found that neurons in the visual cortex of ~5-month-old hAPP-overexpressing mice exhibit aberrant activity. Consistently, we also found increased c-Fos$^+$ cell density in the primary visual cortex compared to WT littermates. To test whether increased c-Fos$^+$ cell density is a general feature of the visual network and brain at large, we performed c-Fos immunohistochemistry on 24 evenly spaced coronal slices spanning the brain of hAPP mice and WT littermate controls and mapped them to the Allen Mouse Brain CCFv3 for regional analysis (Figure 1A-C, see Supplementary Table 1 for region abbreviations). Increases in c-Fos$^+$ cell density were nonuniform in hAPP mice, with posterior dorsal cortical regions showing sharper increases in c-Fos$^+$ cell density (~2-3-fold increase) than thalamic and midbrain regions (~1.1-1.5-fold increase). Notably, the visual cortex displayed, on average, the densest c-Fos$^+$ cells of any region in WT mice (311.4 cells/mm^2) and the largest average magnitude of increased c-Fos$^+$ cell density in hAPP mice (+411.4 cells/mm^2).

We next asked whether aberrant c-Fos$^+$ density patterns are localized to specific layers or subregions of cortical visual areas. Within the primary visual cortex, we found that all layers containing neuronal cell bodies, including layer 4, which receives dense subcortical inputs from

the dorsal part of the lateral geniculate nucleus (Ji et al., 2016; Seabrook et al., 2017), show elevated c-Fos$^+$ cell density in hAPP mice (Supplementary Figure 1). We additionally found that c-Fos$^+$ cell density was significantly higher in most higher-order visual cortical areas in hAPP mice (Figure 1D, Table 2). To test whether subcortical visual network regions upstream of the visual cortex display dense neuronal activation patterns, we next quantified c-Fos$^+$ cell density in the lateral geniculate nucleus and superior colliculus. However, we found no significant difference between hAPP and WT mice in these regions (Figure 1D, Table 2). These results indicate that aberrant patterns of neuronal activation are widespread across cortical but not upstream subcortical areas of the visual system.

To test whether c-Fos expression in the visual system reflects visual experience-evoked neuronal activity, we housed WT and hAPP mice in complete darkness for one week and quantified c-Fos$^+$ cell density. Interestingly, c-Fos$^+$ cell density was significantly increased in WT mice across many areas of the brain (Figure 1C, Table 1), including cortical areas of the visual system (Figure 1D, Table 2). In contrast, c-Fos$^+$ density in hAPP mice was largely unchanged due to visual deprivation. Importantly, the superior colliculus, which receives direct retinal projections (Ito and Feldheim, 2018; Seabrook et al., 2017), uniquely showed reduced c-Fos$^+$ cell density following visual deprivation in both WT and hAPP mice, though this trend did not reach significance for WT mice (Figure 1D, Table 2). Taken together, these results suggest that aberrant c-Fos$^+$ cell density in the visual network is localized to the cortex in early-stage amyloidosis and that c-Fos expression is sensitive to changes in visual experience.

Functional connectivity favors aberrant c-Fos$^+$ cell density across the brain of hAPP mice

Correlated c-Fos$^+$ cell density in a pair of regions indicates functional connectivity between those regions (Silva, Burns and Graff, 2019; Tanimizu et al., 2017; Teles et al., 2015; Vetere et al., 2017; Wheeler et al., 2013). Previous studies have shown that hyperconnectivity is associated

with excessive neuronal activation in early AD networks (Corriveau-Lecavalier et al., 2021; Koelewijn et al., 2019). To confirm whether hAPP mice display hyperconnectivity, we calculated functional connectivity strength for every pair of imaged regions (Pearson's r of c-Fos$^+$ density) both within the visual network and across the brain. Brain-wide (Figure 2A, right) functional connectivity matrices revealed a general increase in pairwise correlation strength between brain regions in hAPP (bottom) relative to WT (top) mice, represented by warmer colors across the hAPP matrices. Similar results were seen for the visual network, though intracortical functional connections were strong even in nonpathological conditions (Figure 2A, left). We quantified this pattern by performing Fisher's r-to-z transformation and calculating the average functional connectivity strength (average z) for each region across its network. We found that nearly all imaged regions exhibited increased average functional connection strength in hAPP networks vs. their WT counterparts (Fig 2B).

Abnormal c-Fos$^+$ cell density, observed in multiple brain regions of hAPP mice (Figure 1C-D), may emerge independently or may arise in part due to the propagation of abnormal activity in other regions via functional connectivity. Thus, we next investigated whether a given region's average network connection strength under nonpathological conditions is predictive of the increase in its c-Fos$^+$ cell density in amyloidosis. We correlated each region's average connection strength across the WT brain-wide or visual network (average z) with the effect size of hAPP overexpression on c-Fos$^+$ density (Cohen's *d*) for that region. A significant positive correlation emerged between these factors, both within the visual (Figure 2C, left) and the whole brain (Figure 2C, right) networks. Furthermore, nonpathological functional connection strength explained ~47% and ~19% of the variance in the effect size of c-Fos$^+$ density in the hAPP visual network and the whole brain, respectively. These results indicate that pre-plaque amyloidosis

induces functional hyperconnectivity and that regions with stronger functional connections across networks in nonpathological conditions are predisposed to elevated c-Fos+ cell density in amyloid pathology.

Amyloidosis selectively weakens an excitatory presynaptic terminal subtype in the visual cortex.

We previously observed functional connectivity alterations that coincide with pro-excitatory structural postsynaptic alterations *in vivo* in layer 2/3 visual cortical neurons of pre-plaque J20-hAPP mice (Niraula et al., 2023). To test whether pro-excitatory presynaptic structural changes also occur in the visual cortex in this model, we first immunolabeled excitatory presynaptic vesicular transporters (VGluT1 and VGluT2) and inhibitory presynaptic vesicular transporters (VGAT) in two visual network regions: the primary visual cortex and the dorsal part of the lateral geniculate nucleus. Automated puncta identification (Figure 3A) revealed a significant decrease in VGluT1$^+$, but not VGluT2$^+$ or VGAT$^+$ puncta densities in the primary visual cortex (with elevated c-Fos expression, Figure 1D, Table 2) of hAPP mice, while the dorsal part of the lateral geniculate nucleus (without significant c-Fos elevation, Figure 1C) showed no significant changes in puncta densities (Figure 3B-D). Note that the puncta densities do not reflect the absolute number of synapses but rather indicate relative differences between genotypes.

Weakening of synapses within a brain region may be represented by loss of presynaptic termini or by shrinking/dimming of termini still present. To test whether detected presynaptic puncta are dimmer in the visual cortex of hAPP mice, we plotted cumulative frequency distributions of the brightness of each individual VGluT1$^+$, VGluT2$^+$, and VGAT$^+$ punctum (Figure 3E-G). VGluT1$^+$, but not VGluT2$^+$ or VGAT$^+$ puncta, tended to be dimmer in the visual cortex of hAPP mice, though this comparison did not reach statistical significance ($p = 0.08$).

Together, these results suggest that amyloidosis is associated with selective weakening of excitatory VGluT1$^+$ presynaptic terminals in the visual cortex.

Amyloidosis induces morphology-specific weakening and loss of excitatory presynaptic boutons *in vivo* but does not influence short-term dynamics.

Though the decrease in detectable immunolabeled VGlut1$^+$ puncta is indicative of excitatory synapse loss in the visual cortex, the dense labeling of VGlut1 antibody limits our analysis to puncta that are brighter than a local threshold. To further confirm that early amyloidosis induces excitatory presynaptic loss in the visual cortex, we analyzed the density and dynamics of presynaptic boutons from the datasets of excitatory layer 2/3 visual cortical neurons imaged *in vivo* using two-photon microscopy. Neurons were imaged in two sessions one week apart, and axons were manually identified by shaft morphology and absence of labeled postsynaptic structures (Figure 4A). We counted presynaptic boutons >3 standard deviations brighter than the axonal shaft and manually classified them as en passant or terminaux (Figure 4B). We found that en passant bouton density in hAPP mice was not different from WT mice (Figure 4C, left), but terminaux bouton density was significantly reduced (Figure 4C, right). However, en passant boutons were dimmer (Figure 4D, left), while terminaux bouton fluorescence did not differ (Figure 4D, right). These results are consistent with VGluT1 immunostaining and indicate that excitatory presynaptic terminals are weakened or lost in amyloidosis.

To test whether the structural dynamics of presynaptic boutons are altered in amyloidosis, we calculated the gain and loss of boutons between the two imaging sessions (Figure 4E). The percentage of stable, gained, and lost boutons were similar between the genotypes for both en passant and terminaux boutons (Figure 4F-H). Furthermore, en passant and terminaux boutons present in both imaging sessions showed no alterations in their brightness between the sessions (Figure 4I). These results suggest that the loss of boutons of layer 2/3 visual cortical neurons

occurs at an earlier age or that bouton loss occurs gradually enough to be undetectable over a one-week period.

Discussion

Here, we show that cortical areas of the visual system are affected early in a model of amyloidosis, exhibiting sharp increases in c-Fos$^+$ cells. Interestingly, the highest increases in c-Fos$^+$ cell density occur in posterior cortical brain regions (visual, retrosplenial, and parietal cortices) that develop high amyloid plaque density at an older age in this mouse model (Whitesell et al., 2019). Pre-plaque mouse models have repeatedly shown that increased amyloid is associated with accelerated calcium transients and calcium dyshomeostasis (Arbel-Ornath et al., 2017; Asavapanumas et al., 2019; Bai et al., 2017; Brawek and Garaschuk, 2014; Busche et al., 2012; Calvo-Rodriguez and Bacskai, 2021; Chakroborty et al., 2012; Lerdkrai et al., 2018; Zhang et al., 2015). Altered calcium dynamics may in turn, alter c-Fos expression through Ras-mitogen-associated protein kinase, calcium/calmodulin-dependent protein kinases, or calcineurin-mediated signaling pathways (Yap and Greenberg, 2018). If visual experience evoked activity contributed to c-Fos$^+$ cell density, then we reasoned that manipulation of visual experience would alter this density. Acute visual deprivation of nonpathological rodents (≤3 days) results in a trend toward mildly reduced visual cortical c-Fos$^+$ cell density, likely as a direct result of the absence of vison-evoked activity (Torrado Pacheco et al., 2019). However, prolonged visual deprivation (≥5 days) triggers reorganization of visual circuits in adult rodents, including increased NR2b/NR2a ratio, reduced GluR2/GABA$_A$ ratio (He, Hodos and Quinlan, 2006), and retraction of inhibitory dendrites or synapses (Chen et al., 2011; Keck et al., 2011; van Versendaal et al., 2012), which together may lower the threshold for neuronal activation (Bridi et al., 2018). Additionally, we recently found that one week of visual deprivation elicited accelerated inhibitory synapse loss in WT mice but not hAPP mice (Niraula, Yan and

Subramanian, 2023). Here, we found that c-Fos$^+$ cell density consistently and sharply increased in WT but not hAPP mice. Together, changes in c-Fos$^+$ cell density (and lack thereof in hAPP mice) due to altered experience are indicative of c-Fos levels representing altered neuronal activity.

Under normal visual experience, c-Fos$^+$ cell density is increased in multiple brain regions in hAPP mice compared to WT mice. Neuronal hyperactivity may emerge independently in different brain regions due to localized instances of imbalanced synaptic excitation and inhibition (Bi et al., 2020; Maestu et al., 2021; Petrache et al., 2019; Ruiter, Herstel and Wierenga, 2020; Vico Varela, Etter and Williams, 2019), potentially leading to higher c-Fos$^+$ cell density. However, in both AD patients and mouse models of amyloidosis, there is considerable heterogeneity in the extent and type of synaptic disruption across brain regions (Berchtold et al., 2013; Kirvell, Esiri and Francis, 2006; Kurucu et al., 2022; Tannenberg et al., 2006). The interconnected nature of brain networks allows for hyperactivity to spread to multiple brain regions without requiring local synaptic disruption. Therefore, variations in the extent of increased c-Fos$^+$ cell density may partly be attributable to variations in functional connectivity of brain regions. A hub region with stronger functional connectivity may display a larger increase in c-Fos$^+$ cell density compared to a brain region with weaker functional connectivity. Consistently, we found that functional connectivity in WT mice can predict ~47% of the variance in effect sizes of hAPP overexpression on c-Fos$^+$ cell density increases, indicating that at least a part of the increase in c-Fos$^+$ cells in these regions could stem from the spread of aberrant activity through functional connections.

Highly functionally connected hub regions may be particularly vulnerable to propagated aberrant activity, triggering a cascade of functional and structural disruption. Functional

connectivity positively correlates with amyloid levels across the brain in humans (Sepulcre et al., 2017). Neuronal hyperactivity promotes local amyloid accumulation (Cirrito et al., 2005; Jones et al., 2016; Leal et al., 2017; Stargardt, Swaab and Bossers, 2015; Yamamoto et al., 2015), which in turn promotes hyperactivity (Bero et al., 2011; Fogel et al., 2014; Harris et al., 2020; Kazim et al., 2017; Kazim et al., 2021; Mattson et al., 1992; Targa Dias Anastacio, Matosin and Ooi, 2022) in a vicious cycle (Zott et al., 2019). Synaptic failure, an eventual outcome of amyloid pathology, is ameliorated by reducing neuronal hyperactivity, resulting in improved memory (Haberman, Branch and Gallagher, 2017; Sanchez et al., 2012). These observations indicate that randomly generated transient hyperactivity in or propagated to hub regions may contribute to idiopathic AD when stabilized by this vicious cycle.

Increases and decreases in synaptic density are likely to enhance and reduce regional neuronal activity, respectively, potentially contributing to or compensating for local aberrant neuronal activity under pathogenic conditions. Using *in vivo* calcium transient imaging and multiphoton structural imaging of postsynaptic structures in the visual cortex of hAPP mice, we recently found neuronal hyperactivity alongside a pro-excitatory shift in the ratio of excitatory to inhibitory postsynaptic structures (Niraula et al., 2023), which presumably would be accompanied by pro-excitatory shifts in presynaptic structures in the form of increased VGluT1/2^{+} puncta and/or decreased VGAT^{+} puncta density. However, we found that VGluT1^{+} puncta are reduced in the visual cortex of hAPP mice. This finding is consistent with a recent study showing reduced terminaux bouton density but unaltered postsynaptic spine density in the barrel cortex of the same mouse model (Stephen et al., 2019). A reduction in presynaptic structure density but normal or elevated postsynaptic structure density indicates that each presynaptic structure may be associated with multiple postsynaptic structures. Thus, early stages

of amyloidosis could be associated with an increase in multi-synaptic boutons (Martinez-Serra et al., 2022).

Presynaptic termini are highly vulnerable at the initial stages of amyloid accumulation (Barthet and Mulle, 2020; de Wilde et al., 2016; Hark et al., 2021; He et al., 2019; Russell et al., 2012; Sze et al., 2000; Trujillo-Estrada et al., 2014). Reduced excitatory presynaptic density has repeatedly been shown to accompany amyloid pathology (Bell, Bennett and Cuello, 2007; Canas et al., 2014; Kashani et al., 2008; Kirvell, Esiri and Francis, 2006; Mitew et al., 2013; Mucke et al., 2000; Naito et al., 2017). Inhibitory synapses have also been shown to be vulnerable to amyloid toxicity, but the results are inconsistent (Agarwal, Tannenberg and Dodd, 2008; Canas et al., 2014; Hollnagel et al., 2019; Kurucu et al., 2022; Mitew et al., 2013; Naito et al., 2017; Niraula et al., 2023; Palop et al., 2007; Ruiter, Herstel and Wierenga, 2020; Verret et al., 2012). Across excitatory synapses, we found VGluT1$^+$ structures to be more vulnerable than VGluT2$^+$ structures in amyloid pathology. One possible cause could be higher amyloid accumulation in VGluT1$^+$ boutons than in VGluT2$^+$ boutons (Sokolow et al., 2012). An alternative possibility is that VGluT1$^+$ puncta predominantly reflect presynaptic termini from cortical neurons, which display elevated c-Fos$^+$ cell density, whereas VGluT2$^+$ structures in the mammalian visual cortex represent projections of the dorsal lateral geniculate nucleus, which in contrast does not show significant changes to c-Fos$^+$ cell density (Balaram, Hackett and Kaas, 2013; Balaram, Takahata and Kaas, 2011; Garcia-Marin et al., 2013; Nahmani and Erisir, 2005).

Structural characterization of presynaptic boutons *in vivo* in layer 2/3 excitatory visual cortical neurons confirmed excitatory bouton loss and revealed morphology-specific alterations induced by amyloidosis. Visual cortical bouton density and rates of seven-day dynamics were similar to those reported in other areas of the mouse neocortex, but some region-specific

variation has been observed (Fulopova et al., 2022; Lees, Johnson and Ashby, 2019). En passant boutons appear dimmer in hAPP mice but are equally dense, whereas terminaux boutons are sparser without appearing dimmer in hAPP neurons. This pattern suggests that when faced with local hyperactivity, en passant boutons may shrink in size while remaining more resilient against complete loss than terminaux boutons. Because no differences were observed in bouton dynamics over one week between hAPP and WT mice, these changes may have primarily occurred at an early time point, or they may emerge slowly over longer time periods. Though functional differences between en passant and terminaux boutons are not well understood, morphology-based modeling suggests that boutons on extremely small terminal branches are especially sensitive to changes in membrane potential (Luscher and Shiner, 1990). Additionally, terminaux boutons are less likely than en passant boutons to harbor mitochondria, which are more commonly found in stable boutons than unstable boutons (Lees, Johnson and Ashby, 2019). Taken together, these results indicate that presynaptic termini carry specific vulnerabilities in amyloidosis based on excitatory/inhibitory status, region of origin, and morphology.

Materials and Methods

Mice

All animal procedures are approved by the University of Kansas Institute of Animal Use and Care Committee and meet the NIH guidelines for the use and care of vertebrate animals. PDGF-hAPP transgenic mice (J20 line; Gladstone) were maintained as heterozygotes for the hAPP transgene by breeding heterozygous J20-hAPP male mice with WT female mice. A maximum of five mice were housed in a standard cage but individually housed after the cranial window surgery. Mice were housed on a 12h-light/12h-dark cycle except for the group that went through a period of visual deprivation (24h-dark). For visual deprivation, mice were placed in a

ventilated, lightproof cabinet inside of a dark room for seven days. Infrared goggles with a low-intensity 850nm wavelength emission source were used at all times while maintaining mice in dark housing to prevent all visual experiences. All mice used for c-Fos immunohistochemistry were housed with 2-3 littermates.

Tissue Preparation and Immunohistochemistry

Mouse cages were brought to the surgical suite and remained undisturbed for at least five hours before brain extractions to avoid capturing c-Fos expression elicited by cage movement or contextual novelty. Dark-housed mice were brought to the surgical suite in a light-blocking container and anesthetized in a dark room using infrared goggles to prevent vision evoked c-Fos expression. 3.5-6-month-old (presynaptic terminal immunohistochemistry) or 5-6-month-old (c-Fos immunohistochemistry) J20-hAPP and WT littermate mice were deeply anesthetized by intraperitoneal injection of 2% avertin in phosphate-buffered saline (PBS), pH 7.4 and transcardially perfused with cold PBS followed by 4% paraformaldehyde. The brains were extracted and post-fixed in 4% PFA overnight at 4°C, followed by storage in PBS. For 40µm slicing, the brains were embedded in 4% oxidized agarose as previously described(Ragan et al., 2012) to limit artifacts during sectioning and sliced on a vibratome (Leica VT1000 S). For 20µm slicing, brains were cryoprotected overnight at 4°C in 15% (w/v) and then in 30% (w/v) sucrose in phosphate buffer (PB). The brains were sectioned coronally on a microtome (Leica SM 2010R) and collected in PBS with sodium azide (0.02%).

24 evenly spaced 40µm slices from each brain spanning the posterior midbrain to the anterior olfactory bulb were fluorescently immunolabeled for c-Fos, and 3 evenly spaced 20-40µm slices spanning the visual cortex and dorsal part of the lateral geniculate nucleus (1-2 slices for each region per mouse) were fluorescently immunolabeled for $VGAT^+$, $VGluT1^+$, and $VGluT2^+$ puncta. Sections were permeabilized for 2h at room temperature in a 1% TritonX-100

and 10% normal goat serum (NGS) solution in PBS followed by incubation with rabbit anti-c-Fos (1:1000, CST) or rabbit anti-VGAT (1:1000, Synaptic Systems), mouse anti-VgluT1 (1:2000, Sigma), and guinea pig anti-VgluT2 (1:1000, Sigma) in a PBS solution containing 0.1% TritonX-100 and 5% NGS overnight at 4°C. Sections were then washed 3× with PBS and incubated with Alexa 555-conjugated goat anti-rabbit antibody (1:2000; Fisher) for c-Fos immunohistochemistry or Alexa 488 conjugated goat anti-rabbit antibody (1:2000, Fisher), Alexa 555-conjugated goat anti-mouse antibody (1:2000, Fisher), and Alexa 647-conjugated goat anti-guinea pig antibody (1:2000, Fisher) for presynaptic terminal immunohistochemistry for two hours in a PBS solution containing 0.1% TritonX-100 and 5% NGS at room temperature, followed by three washes with PBS before mounting on glass slides. Slices were imaged using an ImageXpress Pico automated imaging system (Molecular Devices, San Jose, CA) with a 10× objective for c-Fos acquisition (Leica HC PL FLUOTAR 10x/0.32) or a 63× objective for presynaptic termini acquisition (Leica HC PL FLUOTAR 63x/0.70 CORR).

Immunofluorescence Quantification and Statistical Analysis

Slice registration, cell/synapse detection, puncta fluorescence collection, and brain region area measurements were performed using NeuroInfo software (MBF Bioscience, Williston, VT). 12-bit slice images were first mapped in 3D to the Allen CCF v3 to allow automated cell/synapse detection and area measurement by region. A total of 31 regions covering the entire cerebral cortex, cerebral nuclei, interbrain, and midbrain, and 17 subregions of the visual network were mapped for analysis. Bright circular objects against a darker background were automatically detected using a scale-space analysis of the response to Laplacian of Gaussian (LoG) within the expected range of labeled cell body or presynaptic puncta diameters as described (Kong, Akakin and Sarma, 2013). Briefly, cells/synapses were filtered out from all identified objects with a user-defined threshold based on the strength of the LoG response within an expected range of

cell body or presynaptic terminal diameters. The LoG threshold value was set at LoG threshold = 55 for cell bodies and 101 for all presynaptic puncta (range 0-255). Only objects above the respective LoG strength threshold were included in the analysis, and identified objects were manually proofread to eliminate false positives. All regions in both hemispheres of the 24 brain-wide slices were analyzed for c-Fos$^+$ cell detection. Cell/synaptic puncta density for each mouse was calculated by dividing the total number of cells or synapses per region by the area per region across all slices for each brain (24 slices for c-Fos, 2-3 slices for synapses). Pearson's r was calculated between each pairwise combination of brain regions either within the whole brain or visual network for light and dark conditions, and average z values were calculated following Fisher's r-to-z transformation for each region within its respective network. 8 WT light (6 males, 2 females), 7 WT dark (2 males, 5 females), 9 hAPP light (4 males, 5 females), and 6 hAPP dark housed mice (1 male, 5 females) were used for c-Fos$^+$ cell density analysis.

For presynaptic terminal quantification, 1-2 ~230 × 900µm columns per mouse spanning all layers of one hemisphere of the visual cortex was analyzed, and 1-2 ~230 × 375µm columns per mouse vertically spanning one hemisphere of the dorsal lateral geniculate nucleus were analyzed. Synaptic puncta fluorescence was determined by collecting the fluorescence from a 0.2µm (1.9 pixel) radius around the center of each identified puncta. Localized areas containing artifacts were excluded from the analysis. 14 WT (9 males, 5 females) and 12 hAPP mice (6 males, 6 females) were used for presynaptic density and fluorescence analysis. Synaptic puncta fluorescence analysis in the visual cortex included a total of 759,230 WT & 550,683 hAPP VGAT$^+$ puncta, 386,322 WT & 223,032 hAPP VGluT1$^+$ puncta, and 330,103 WT & 239,168 hAPP VGluT2$^+$ puncta. Representative images were generated in FIJI (NIH, Bethesda, MD), and

all figures and statistical tests were performed in GraphPad Prism (GraphPad Software, San Diego, CA).

In Vivo Presynaptic Structural Analysis

The presented in vivo presynaptic structural data is an independent analysis performed from the same raw dataset acquired as previously described (Niraula et al., 2023a; Niraula et al., 2023b). TdTomato-filled axons were first identified based on branch morphology and absence of postsynaptic markers, then en passant and terminaux boutons were manually labeled based on morphology using a modified version of the ObjectJ plugin (Villa et al., 2016) for FIJI (Schindelin et al., 2012). Puncta on or protruding from axonal shafts were scored as boutons only if they were present in two consecutive z-frames. After proofreading of the bouton identification and classification in both sessions by another investigator, the marked boutons were subjected to an unbiased intensity-based threshold relative to the nearby axonal shaft. 5-pixel × 5-pixel measurement ROIs were placed over the identified boutons and along their respective axonal shafts, and the fluorescent intensity of each bouton and its nearest 10-20 neighboring axonal shaft ROIs were collected using the modified ObjectJ plugin. Using the modified ObjectJ plugin, bouton IDs and locations were transferred from S1 to S2 image stacks, and newly formed and lost boutons were manually identified. Identified objects were excluded if their fluorescence did not exceed three times the standard deviation of fluorescence of the nearest neighboring axonal shaft ROIs. Bouton gain and loss were calculated as the number of gained or lost boutons between S1 and S2 divided by the number of boutons present in S1. The percentage of stable boutons was calculated as the number of boutons that persisted into S2 divided by the number of boutons in S1. The percentage of fluorescence change in stable boutons between S1 and S2 was calculated as S2 fluorescence divided by S1 fluorescence for each stable bouton where a bouton's fluorescence is represented by the number of standard deviations above the average fluorescence

of the nearest 10-20 neighboring shaft ROIs in its respective session. Nearest neighbor and threshold calculations were performed using custom MATLAB scripts. All bouton metrics were calculated separately for en passant and terminaux boutons. All in vivo bouton data was obtained from 7 WT cells (4 mice, 2 males and 2 females) and 8 hAPP cells (7 mice, 5 males and 2 females). For S1 bouton fluorescence distribution, a total of 347 en passant and 62 terminaux boutons were identified from WT cells, and 287 en passant & 19 terminaux boutons were identified from hAPP cells.

Figure Legends

Figure 1: **c-Fos$^+$ cell density increases due to hAPP overexpression or one week of dark housing. A)** Representative images of 24 evenly spaced landmark slices used for brain-wide c-Fos$^+$ cell density quantification. **B)** Representative images of c-Fos fluorescence in the primary visual cortex of hAPP mice (right) and wildtype (WT) littermate controls (left). The blue box is zoomed in on each right panel. Blue circles indicate c-Fos$^+$ cells identified by automatic cell detection. The identification threshold was set such that very dim cells representing close to baseline c-Fos expression were excluded. Scale bar: 1mm (left half of each panel), 100µm (right half). **C)** c-Fos$^+$ cell density across the brain for hAPP and WT mice under a standard 12h light/dark cycle (Light) and one week of visual deprivation (Dark). See Table 1 for mixed-effects ANOVA results. **D)** c-Fos$^+$ cell density across regions of the visual network for hAPP and WT mice under a standard 12h light/dark cycle (Light) and one week of visual deprivation (Dark). See Table 2 for mixed-effects ANOVA results. Data are presented as mean ± SEM. n = 8 WT light, 7 WT dark, 9 hAPP light, and 6 hAPP dark housed mice.

Figure 2: **WT functional connectivity correlates with regional c-Fos$^+$ density increases due to hAPP overexpression or prolonged visual deprivation. A)** Functional connectivity matrices showing pairwise correlation (Pearson's *r*) of c-Fos$^+$ density between regions in the visual (left)

and the brain-wide (right) networks for WT (top) and hAPP (bottom) mice. Region label color indicates anatomical brain area. Warmer colors indicate stronger pairwise functional connections between regions. B**)** Each region's average correlation strength (average z following r-to-z transformation) across the visual (left) and whole brain (right) networks in WT and hAPP mice. Paired *t*-tests, ****p-value < 0.0001. n = 8 WT, 9 hAPP mice. C) Correlation of each region's average z across WT networks (visual, left; whole brain, right) with the effect size (Cohen's *d*) of hAPP on c-Fos$^+$ cell density. n = 8 WT, 9 hAPP mice. Linear regression with 95% confidence intervals, correlation p-values, and R^2 are shown.

Figure 3: **Excitatory synapse loss is associated with aberrant c-Fos expression in amyloidosis. A)** Representative images of synaptic immunohistochemistry labeling VGluT1, VGluT2, VGAT, and merged channels in layer 2/3 of the primary visual cortex in WT (top) and hAPP (bottom) mice. Circles indicate puncta identified by automated synapse detection. Some circles contain dim puncta that have sufficient fluorescence above local background to meet the detection threshold. Scale bar: 10µm (merge), 5µm (individual channels). **B-D)** Density of VGluT1$^+$ (B), VGluT2$^+$ (C), and VGAT$^+$ (D) puncta in the primary visual cortex (VISp) and dorsal part of the lateral geniculate nucleus (dLGN). **E-G)** Cumulative frequency distributions of individual VGluT1$^+$ (E), VGluT2$^+$ (F), and VGAT$^+$ (G) puncta fluorescence in arbitrary units (AU). Kolmogorov-Smirnov tests, p-values displayed. n = 14 WT, 12 hAPP mice (VISp). n = 13 WT, 11 hAPP mice (dLGN).

Figure 4: **Amyloidosis induces excitatory terminaux bouton loss in L2/3 of the primary visual cortex *in vivo*. A)** Experimental timeline for *in vivo* presynaptic structural imaging. Imaging sessions (S1 and S2) were separated by one week. **B)** Representative *in vivo* image of presynaptic boutons of excitatory layer 2/3 primary visual cortical neurons in WT (top) and

hAPP mice (bottom). Example terminaux (filled arrowhead) and en passant (open arrowhead) boutons. Scale bar: 5µm. **C)** En passant (left) and terminaux (right) bouton density of excitatory layer 2/3 primary visual cortical neurons. **D)** Cumulative frequency distributions of S1 en passant (left) and terminaux (right) bouton brightness, represented as number of standard deviations above nearby axonal shaft fluorescence. Kolmogorov-Smirnov tests, p-values displayed. **E)** Representative images of boutons that are gained (left, filled arrowhead) and lost (right, open arrowhead) between imaging sessions. Scale bar: 2µm. **F-I)** En passant (left) and terminaux (right) bouton dynamics, including percent stable (F), gained (G), lost (H), and fluorescence change (I) of boutons in S2 relative to S1. Data are presented as mean ± SEM, individual data points represent cell averages. student's *t*-tests, *p-value < 0.05. n = 7 cells from 4 WT mice, 8 cells from 7 hAPP mice for all.

Competing interests: The authors declare no competing interests.

Author contributions: OJL, ASS and JS designed the experiments and analysis. OJL, JM, SN and GD performed the experiments and analyzed the data. OJL and JS wrote the manuscript. JS supervised the research.

Acknowledgements

We thank the Subramanian lab members for their help with revising this manuscript. This work was supported by a grant from the National Institutes of Health (Grant No. RO1AG064067) to JS.

References

Agarwal, S., Tannenberg, R. K., Dodd, P. R., 2008. Reduced expression of the inhibitory synapse scaffolding protein gephyrin in Alzheimer's disease. J Alzheimers Dis. 14**,** 313-21.

Arbel-Ornath, M., et al., 2017. Soluble oligomeric amyloid-beta induces calcium dyshomeostasis that precedes synapse loss in the living mouse brain. Mol Neurodegener. 12**,** 27.

Armstrong, R. A., 2009. Alzheimer's Disease and the Eye☆. Journal of Optometry. 2**,** 103-111.

Asavapanumas, N., et al., 2019. Role of intracellular Ca(2+) stores for an impairment of visual processing in a mouse model of Alzheimer's disease. Neurobiol Dis. 121**,** 315-326.

Bai, Y., et al., 2017. Abnormal dendritic calcium activity and synaptic depotentiation occur early in a mouse model of Alzheimer's disease. Mol Neurodegener. 12**,** 86.

Balaram, P., Hackett, T. A., Kaas, J. H., 2013. Differential expression of vesicular glutamate transporters 1 and 2 may identify distinct modes of glutamatergic transmission in the macaque visual system. J Chem Neuroanat. 50-51**,** 21-38.

Balaram, P., Takahata, T., Kaas, J. H., 2011. VGLUT2 mRNA and protein expression in the visual thalamus and midbrain of prosimian galagos (Otolemur garnetti). Eye Brain. 2011**,** 5-15.

Barth, A. L., Gerkin, R. C., Dean, K. L., 2004. Alteration of neuronal firing properties after in vivo experience in a FosGFP transgenic mouse. J Neurosci. 24**,** 6466-75.

Barthet, G., Mulle, C., 2020. Presynaptic failure in Alzheimer's disease. Prog Neurobiol. 194**,** 101801.

Beach, T. G., Walker, R., McGeer, E. G., 1989. Lamina-selective A68 immunoreactivity in primary visual cortex of Alzheimer's disease patients. Brain Res. 501**,** 171-4.

Bell, K. F., Bennett, D. A., Cuello, A. C., 2007. Paradoxical upregulation of glutamatergic presynaptic boutons during mild cognitive impairment. J Neurosci. 27**,** 10810-7.

Berchtold, N. C., et al., 2013. Synaptic genes are extensively downregulated across multiple brain regions in normal human aging and Alzheimer's disease. Neurobiol Aging. 34**,** 1653-61.

Bero, A. W., et al., 2011. Neuronal activity regulates the regional vulnerability to amyloid-beta deposition. Nat Neurosci. 14**,** 750-6.

Best, J., Chapleau, M., Rabinovici, G. D., 2023. Posterior cortical atrophy: clinical, neuroimaging, and neuropathological features. Expert Rev Neurother. 23**,** 227-236.

Bi, D., et al., 2020. GABAergic dysfunction in excitatory and inhibitory (E/I) imbalance drives the pathogenesis of Alzheimer's disease. Alzheimers Dement. 16**,** 1312-1329.

Borcuk, C., et al., 2022. Early memory deficits and extensive brain network disorganization in the App(NL-F)/MAPT double knock-in mouse model of familial Alzheimer's disease. Aging Brain. 2**,** 100042.

Brawek, B., Garaschuk, O., 2014. Network-wide dysregulation of calcium homeostasis in Alzheimer's disease. Cell Tissue Res. 357**,** 427-38.

Bridi, M. C. D., et al., 2018. Two distinct mechanisms for experience-dependent homeostasis. Nat Neurosci. 21**,** 843-850.

Busche, M. A., et al., 2012. Critical role of soluble amyloid-beta for early hippocampal hyperactivity in a mouse model of Alzheimer's disease. Proc Natl Acad Sci U S A. 109**,** 8740-5.

Calvo-Rodriguez, M., Bacskai, B. J., 2021. Mitochondria and Calcium in Alzheimer's Disease: From Cell Signaling to Neuronal Cell Death. Trends Neurosci. 44**,** 136-151.

Canas, P. M., et al., 2014. Predominant loss of glutamatergic terminal markers in a beta-amyloid peptide model of Alzheimer's disease. Neuropharmacology. 76 Pt A, 51-6.
Chakroborty, S., et al., 2012. Early presynaptic and postsynaptic calcium signaling abnormalities mask underlying synaptic depression in presymptomatic Alzheimer's disease mice. J Neurosci. 32, 8341-53.
Chen, C., et al., 2022. Early impairment of cortical circuit plasticity and connectivity in the 5XFAD Alzheimer's disease mouse model. Transl Psychiatry. 12, 371.
Chen, J. L., et al., 2011. Structural basis for the role of inhibition in facilitating adult brain plasticity. Nat Neurosci. 14, 587-94.
Chen, Y., et al., 2019. Neural Mechanisms of Visual Dysfunction in Posterior Cortical Atrophy. Front Neurol. 10, 670.
Chiquita, S., et al., 2019. Retinal thinning of inner sub-layers is associated with cortical atrophy in a mouse model of Alzheimer's disease: a longitudinal multimodal in vivo study. Alzheimers Res Ther. 11, 90.
Cirrito, J. R., et al., 2005. Synaptic activity regulates interstitial fluid amyloid-beta levels in vivo. Neuron. 48, 913-22.
Cormack, F. K., Tovee, M., Ballard, C., 2000. Contrast sensitivity and visual acuity in patients with Alzheimer's disease. Int J Geriatr Psychiatry. 15, 614-20.
Corriveau-Lecavalier, N., et al., 2021. Latent patterns of task-related functional connectivity in relation to regions of hyperactivation in individuals at risk of Alzheimer's disease. Neuroimage Clin. 30, 102643.
Criscuolo, C., et al., 2018. The retina as a window to early dysfunctions of Alzheimer's disease following studies with a 5xFAD mouse model. Neurobiol Aging. 67, 181-188.
Crowe, S. E., Ellis-Davies, G. C., 2014. Spine pruning in 5xFAD mice starts on basal dendrites of layer 5 pyramidal neurons. Brain Struct Funct. 219, 571-80.
Crutch, S. J., et al., 2012. Posterior cortical atrophy. Lancet Neurol. 11, 170-8.
Cui, J. G., et al., 2007. Expression of inflammatory genes in the primary visual cortex of late-stage Alzheimer's disease. Neuroreport. 18, 115-9.
de Wilde, M. C., et al., 2016. Meta-analysis of synaptic pathology in Alzheimer's disease reveals selective molecular vesicular machinery vulnerability. Alzheimers Dement. 12, 633-44.
Fogel, H., et al., 2014. APP homodimers transduce an amyloid-beta-mediated increase in release probability at excitatory synapses. Cell Rep. 7, 1560-1576.
Frisoni, G. B., et al., 2009. In vivo mapping of incremental cortical atrophy from incipient to overt Alzheimer's disease. J Neurol. 256, 916-24.
Fulopova, B., et al., 2022. Cortical axon sub-population maintains density, but not turnover, of en passant boutons in the aged APP/PS1 amyloidosis model. Neurobiol Aging. 115, 29-38.
Garcia-Marin, V., et al., 2013. Distribution of vesicular glutamate transporter 2 (VGluT2) in the primary visual cortex of the macaque and human. J Comp Neurol. 521, 130-51.
Gour, N., et al., 2014. Functional connectivity changes differ in early and late-onset Alzheimer's disease. Hum Brain Mapp. 35, 2978-94.
Grienberger, C., et al., 2012. Staged decline of neuronal function in vivo in an animal model of Alzheimer's disease. Nat Commun. 3, 774.
Guenthner, C. J., et al., 2013. Permanent genetic access to transiently active neurons via TRAP: targeted recombination in active populations. Neuron. 78, 773-84.

Haberman, R. P., Branch, A., Gallagher, M., 2017. Targeting Neural Hyperactivity as a Treatment to Stem Progression of Late-Onset Alzheimer's Disease. Neurotherapeutics. 14**,** 662-676.
Hao, J., et al., 2005. Visual attention deficits in Alzheimer's disease: an fMRI study. Neurosci Lett. 385**,** 18-23.
Hark, T. J., et al., 2021. Pulse-Chase Proteomics of the App Knockin Mouse Models of Alzheimer's Disease Reveals that Synaptic Dysfunction Originates in Presynaptic Terminals. Cell Syst. 12**,** 141-158 e9.
Harris, S. S., et al., 2020. Tipping the Scales: Peptide-Dependent Dysregulation of Neural Circuit Dynamics in Alzheimer's Disease. Neuron. 107**,** 417-435.
He, H. Y., Hodos, W., Quinlan, E. M., 2006. Visual deprivation reactivates rapid ocular dominance plasticity in adult visual cortex. J Neurosci. 26**,** 2951-5.
He, Y., et al., 2019. Amyloid beta oligomers suppress excitatory transmitter release via presynaptic depletion of phosphatidylinositol-4,5-bisphosphate. Nat Commun. 10**,** 1193.
Hill, J. M., et al., 2014. An evaluation of progressive amyloidogenic and pro-inflammatory change in the primary visual cortex and retina in Alzheimer's disease (AD). Front Neurosci. 8**,** 347.
Hof, P. R., Morrison, J. H., 1990. Quantitative analysis of a vulnerable subset of pyramidal neurons in Alzheimer's disease: II. Primary and secondary visual cortex. J Comp Neurol. 301**,** 55-64.
Holden, S. K., Bettcher, B. M., Pelak, V. S., 2020. Update on posterior cortical atrophy. Curr Opin Neurol. 33**,** 68-73.
Hollnagel, J. O., et al., 2019. Early alterations in hippocampal perisomatic GABAergic synapses and network oscillations in a mouse model of Alzheimer's disease amyloidosis. PLoS One. 14**,** e0209228.
Hwang, J., et al., 2021. Clinical Implications of Amyloid-Beta Accumulation in Occipital Lobes in Alzheimer's Continuum. Brain Sci. 11.
Ikonomovic, M. D., et al., 2005. Reduction of choline acetyltransferase activity in primary visual cortex in mild to moderate Alzheimer's disease. Arch Neurol. 62**,** 425-30.
Ito, S., Feldheim, D. A., 2018. The Mouse Superior Colliculus: An Emerging Model for Studying Circuit Formation and Function. Front Neural Circuits. 12**,** 10.
Ji, X. Y., et al., 2016. Thalamocortical Innervation Pattern in Mouse Auditory and Visual Cortex: Laminar and Cell-Type Specificity. Cereb Cortex. 26**,** 2612-25.
Jones, D. T., et al., 2016. Cascading network failure across the Alzheimer's disease spectrum. Brain. 139**,** 547-62.
Jorge, L., et al., 2020. The Retinal Inner Plexiform Synaptic Layer Mirrors Grey Matter Thickness of Primary Visual Cortex with Increased Amyloid beta Load in Early Alzheimer's Disease. Neural Plast. 2020**,** 8826087.
Kashani, A., et al., 2008. Loss of VGLUT1 and VGLUT2 in the prefrontal cortex is correlated with cognitive decline in Alzheimer disease. Neurobiol Aging. 29**,** 1619-30.
Kawashima, T., Okuno, H., Bito, H., 2014. A new era for functional labeling of neurons: activity-dependent promoters have come of age. Front Neural Circuits. 8**,** 37.
Kazim, S. F., et al., 2017. Early-Onset Network Hyperexcitability in Presymptomatic Alzheimer's Disease Transgenic Mice Is Suppressed by Passive Immunization with Anti-Human APP/Abeta Antibody and by mGluR5 Blockade. Front Aging Neurosci. 9**,** 71.

Kazim, S. F., et al., 2021. Neuronal Network Excitability in Alzheimer's Disease: The Puzzle of Similar versus Divergent Roles of Amyloid beta and Tau. eNeuro. 8.
Keck, T., et al., 2011. Loss of sensory input causes rapid structural changes of inhibitory neurons in adult mouse visual cortex. Neuron. 71**,** 869-82.
Kirby, E., Bandelow, S., Hogervorst, E., 2010. Visual impairment in Alzheimer's disease: a critical review. J Alzheimers Dis. 21**,** 15-34.
Kirvell, S. L., Esiri, M., Francis, P. T., 2006. Down-regulation of vesicular glutamate transporters precedes cell loss and pathology in Alzheimer's disease. J Neurochem. 98**,** 939-50.
Koelewijn, L., et al., 2019. Oscillatory hyperactivity and hyperconnectivity in young APOE-varepsilon4 carriers and hypoconnectivity in Alzheimer's disease. Elife. 8.
Kong, H., Akakin, H. C., Sarma, S. E., 2013. A generalized Laplacian of Gaussian filter for blob detection and its applications. IEEE Trans Cybern. 43**,** 1719-33.
Korzhova, V., et al., 2021. Long-term dynamics of aberrant neuronal activity in awake Alzheimer's disease transgenic mice. Commun Biol. 4**,** 1368.
Kurucu, H., et al., 2022. Inhibitory synapse loss and accumulation of amyloid beta in inhibitory presynaptic terminals in Alzheimer's disease. Eur J Neurol. 29**,** 1311-1323.
Kusne, Y., et al., 2017. Visual system manifestations of Alzheimer's disease. Acta Ophthalmol. 95**,** e668-e676.
Leal, S. L., et al., 2017. Hippocampal activation is associated with longitudinal amyloid accumulation and cognitive decline. Elife. 6.
Lees, R. M., Johnson, J. D., Ashby, M. C., 2019. Presynaptic Boutons That Contain Mitochondria Are More Stable. Front Synaptic Neurosci. 11**,** 37.
Lerdkrai, C., et al., 2018. Intracellular Ca(2+) stores control in vivo neuronal hyperactivity in a mouse model of Alzheimer's disease. Proc Natl Acad Sci U S A. 115**,** E1279-E1288.
Leuba, G., Kraftsik, R., 1994. Visual cortex in Alzheimer's disease: occurrence of neuronal death and glial proliferation, and correlation with pathological hallmarks. Neurobiol Aging. 15**,** 29-43.
Lewis, D. A., et al., 1987. Laminar and regional distributions of neurofibrillary tangles and neuritic plaques in Alzheimer's disease: a quantitative study of visual and auditory cortices. J Neurosci. 7**,** 1799-808.
Liebscher, S., et al., 2016. Selective Persistence of Sensorimotor Mismatch Signals in Visual Cortex of Behaving Alzheimer's Disease Mice. Curr Biol. 26**,** 956-64.
Liu, X., et al., 2012. Optogenetic stimulation of a hippocampal engram activates fear memory recall. Nature. 484**,** 381-5.
Luscher, H. R., Shiner, J. S., 1990. Computation of action potential propagation and presynaptic bouton activation in terminal arborizations of different geometries. Biophys J. 58**,** 1377-88.
Maestu, F., et al., 2021. Neuronal excitation/inhibition imbalance: core element of a translational perspective on Alzheimer pathophysiology. Ageing Res Rev. 69**,** 101372.
Mahringer, D., et al., 2022. Functional correlates of immediate early gene expression in mouse visual cortex. Peer Community J. 2**,** e45.
Maia da Silva, M. N., et al., 2017. Visual Dysfunction in Posterior Cortical Atrophy. Front Neurol. 8**,** 389.
Mandal, P. K., Joshi, J., Saharan, S., 2012. Visuospatial perception: an emerging biomarker for Alzheimer's disease. J Alzheimers Dis. 31 Suppl 3**,** S117-35.

Martinez-Serra, R., et al., 2022. Emerging insights into synapse dysregulation in Alzheimer's disease. Brain Commun. 4, fcac083.
Mattson, M. P., et al., 1992. beta-Amyloid peptides destabilize calcium homeostasis and render human cortical neurons vulnerable to excitotoxicity. J Neurosci. 12, 376-89.
Mavroudis, I. A., et al., 2011. Dendritic pathology and spinal loss in the visual cortex in Alzheimer's disease: a Golgi study in pathology. Int J Neurosci. 121, 347-54.
Maya-Vetencourt, J. F., et al., 2014. Amyloid plaque-independent deficit of early postnatal visual cortical plasticity in the 5XFAD transgenic model of Alzheimer's disease. J Alzheimers Dis. 42, 103-7.
Metsaars, W. P., et al., 2003. A grading system of Alzheimer disease lesions in neocortical areas. Neurobiol Aging. 24, 563-72.
Mitew, S., et al., 2013. Altered synapses and gliotransmission in Alzheimer's disease and AD model mice. Neurobiol Aging. 34, 2341-51.
Morgan, J. I., et al., 1987. Mapping patterns of c-fos expression in the central nervous system after seizure. Science. 237, 192-7.
Morrison, J. H., Hof, P. R., Bouras, C., 1991. An anatomic substrate for visual disconnection in Alzheimer's disease. Ann N Y Acad Sci. 640, 36-43.
Mucke, L., et al., 2000. High-level neuronal expression of abeta 1-42 in wild-type human amyloid protein precursor transgenic mice: synaptotoxicity without plaque formation. J Neurosci. 20, 4050-8.
Murphy, C., 2019. Olfactory and other sensory impairments in Alzheimer disease. Nat Rev Neurol. 15, 11-24.
Nahmani, M., Erisir, A., 2005. VGluT2 immunochemistry identifies thalamocortical terminals in layer 4 of adult and developing visual cortex. J Comp Neurol. 484, 458-73.
Naito, Y., et al., 2017. Amyloid-beta Oligomers Interact with Neurexin and Diminish Neurexin-mediated Excitatory Presynaptic Organization. Sci Rep. 7, 42548.
Niraula, S., et al., 2023. Excitation-inhibition imbalance disrupts visual familiarity in amyloid and non-pathology conditions. Cell Rep. 42, 111946.
Niraula, S., Yan, S. S., Subramanian, J., 2023. Amyloid pathology impairs homeostatic inhibitory synaptic plasticity. bioRxiv.
North, C., et al., 2021. Neuropsychological deficits in Posterior Cortical Atrophy and typical Alzheimer's disease: A meta-analytic review. Cortex. 143, 223-236.
Palop, J. J., et al., 2007. Aberrant excitatory neuronal activity and compensatory remodeling of inhibitory hippocampal circuits in mouse models of Alzheimer's disease. Neuron. 55, 697-711.
Papanikolaou, A., et al., 2022. Plasticity in visual cortex is disrupted in a mouse model of tauopathy. Commun Biol. 5, 77.
Petrache, A. L., et al., 2019. Aberrant Excitatory-Inhibitory Synaptic Mechanisms in Entorhinal Cortex Microcircuits During the Pathogenesis of Alzheimer's Disease. Cereb Cortex. 29, 1834-1850.
Ragan, T., et al., 2012. Serial two-photon tomography for automated ex vivo mouse brain imaging. Nat Methods. 9, 255-8.
Reijmers, L. G., et al., 2007. Localization of a stable neural correlate of associative memory. Science. 317, 1230-3.
Rosales Jubal, E., et al., 2021. Acitretin reverses early functional network degradation in a mouse model of familial Alzheimer's disease. Sci Rep. 11, 6649.

Rudinskiy, N., et al., 2012. Orchestrated experience-driven Arc responses are disrupted in a mouse model of Alzheimer's disease. Nat Neurosci. 15, 1422-9.
Ruiter, M., Herstel, L. J., Wierenga, C. J., 2020. Reduction of Dendritic Inhibition in CA1 Pyramidal Neurons in Amyloidosis Models of Early Alzheimer's Disease. J Alzheimers Dis. 78, 951-964.
Russell, C. L., et al., 2012. Amyloid-beta acts as a regulator of neurotransmitter release disrupting the interaction between synaptophysin and VAMP2. PLoS One. 7, e43201.
Sanchez, P. E., et al., 2012. Levetiracetam suppresses neuronal network dysfunction and reverses synaptic and cognitive deficits in an Alzheimer's disease model. Proc Natl Acad Sci U S A. 109, E2895-903.
Schindelin, J., et al., 2012. Fiji: an open-source platform for biological-image analysis. Nat Methods. 9, 676-82.
Seabrook, T. A., et al., 2017. Architecture, Function, and Assembly of the Mouse Visual System. Annu Rev Neurosci. 40, 499-538.
Sepulcre, J., et al., 2017. Tau and amyloid beta proteins distinctively associate to functional network changes in the aging brain. Alzheimers Dement. 13, 1261-1269.
Silva, B. A., Burns, A. M., Graff, J., 2019. A cFos activation map of remote fear memory attenuation. Psychopharmacology (Berl). 236, 369-381.
Sokolow, S., et al., 2012. Preferential accumulation of amyloid-beta in presynaptic glutamatergic terminals (VGluT1 and VGluT2) in Alzheimer's disease cortex. Neurobiol Dis. 45, 381-7.
Stargardt, A., Swaab, D. F., Bossers, K., 2015. Storm before the quiet: neuronal hyperactivity and Abeta in the presymptomatic stages of Alzheimer's disease. Neurobiol Aging. 36, 1-11.
Stephen, T. L., et al., 2019. Imbalance in the response of pre- and postsynaptic components to amyloidopathy. Sci Rep. 9, 14837.
Sze, C. I., et al., 2000. Selective regional loss of exocytotic presynaptic vesicle proteins in Alzheimer's disease brains. J Neurol Sci. 175, 81-90.
Tanimizu, T., et al., 2017. Functional Connectivity of Multiple Brain Regions Required for the Consolidation of Social Recognition Memory. J Neurosci. 37, 4103-4116.
Tannenberg, R. K., et al., 2006. Selective loss of synaptic proteins in Alzheimer's disease: evidence for an increased severity with APOE varepsilon4. Neurochem Int. 49, 631-9.
Targa Dias Anastacio, H., Matosin, N., Ooi, L., 2022. Neuronal hyperexcitability in Alzheimer's disease: what are the drivers behind this aberrant phenotype? Translational Psychiatry. 12.
Teles, M. C., et al., 2015. Social interactions elicit rapid shifts in functional connectivity in the social decision-making network of zebrafish. Proc Biol Sci. 282, 20151099.
Torrado Pacheco, A., et al., 2019. Rapid and active stabilization of visual cortical firing rates across light-dark transitions. Proc Natl Acad Sci U S A. 116, 18068-18077.
Trujillo-Estrada, L., et al., 2014. Early neuronal loss and axonal/presynaptic damage is associated with accelerated amyloid-beta accumulation in AbetaPP/PS1 Alzheimer's disease mice subiculum. J Alzheimers Dis. 42, 521-41.
van Veluw, S. J., et al., 2020. Vasomotion as a Driving Force for Paravascular Clearance in the Awake Mouse Brain. Neuron. 105, 549-561 e5.
van Versendaal, D., et al., 2012. Elimination of inhibitory synapses is a major component of adult ocular dominance plasticity. Neuron. 74, 374-83.

Verret, L., et al., 2012. Inhibitory interneuron deficit links altered network activity and cognitive dysfunction in Alzheimer model. Cell. 149, 708-21.
Vetere, G., et al., 2017. Chemogenetic Interrogation of a Brain-wide Fear Memory Network in Mice. Neuron. 94, 363-374 e4.
Vico Varela, E., Etter, G., Williams, S., 2019. Excitatory-inhibitory imbalance in Alzheimer's disease and therapeutic significance. Neurobiol Dis. 127, 605-615.
Villa, K. L., et al., 2016. Inhibitory Synapses Are Repeatedly Assembled and Removed at Persistent Sites In Vivo. Neuron. 89, 756-69.
Wang, K., et al., 2007. Altered functional connectivity in early Alzheimer's disease: a resting-state fMRI study. Hum Brain Mapp. 28, 967-78.
Wheeler, A. L., et al., 2013. Identification of a functional connectome for long-term fear memory in mice. PLoS Comput Biol. 9, e1002853.
Whitesell, J. D., et al., 2019. Whole brain imaging reveals distinct spatial patterns of amyloid beta deposition in three mouse models of Alzheimer's disease. J Comp Neurol. 527, 2122-2145.
William, C. M., et al., 2012. Synaptic plasticity defect following visual deprivation in Alzheimer's disease model transgenic mice. J Neurosci. 32, 8004-11.
William, C. M., et al., 2021. Impairment of visual cortical plasticity by amyloid-beta species. Neurobiol Dis. 154, 105344.
Yamamoto, K., et al., 2015. Chronic optogenetic activation augments abeta pathology in a mouse model of Alzheimer disease. Cell Rep. 11, 859-865.
Yap, E. L., Greenberg, M. E., 2018. Activity-Regulated Transcription: Bridging the Gap between Neural Activity and Behavior. Neuron. 100, 330-348.
Yassin, L., et al., 2010. An embedded subnetwork of highly active neurons in the neocortex. Neuron. 68, 1043-50.
Yerstein, O., et al., 2021. Benson's Disease or Posterior Cortical Atrophy, Revisited. J Alzheimers Dis. 82, 493-502.
Zangenehpour, S., Chaudhuri, A., 2002. Differential induction and decay curves of c-fos and zif268 revealed through dual activity maps. Brain Res Mol Brain Res. 109, 221-5.
Zhang, H., et al., 2015. Calcium signaling, excitability, and synaptic plasticity defects in a mouse model of Alzheimer's disease. J Alzheimers Dis. 45, 561-80.
Zhang, N. K., et al., 2023. Sensory processing deficits and related cortical pathological changes in Alzheimer's disease. Front Aging Neurosci. 15, 1213379.
Zott, B., et al., 2019. A vicious cycle of beta amyloid-dependent neuronal hyperactivation. Science. 365, 559-565.

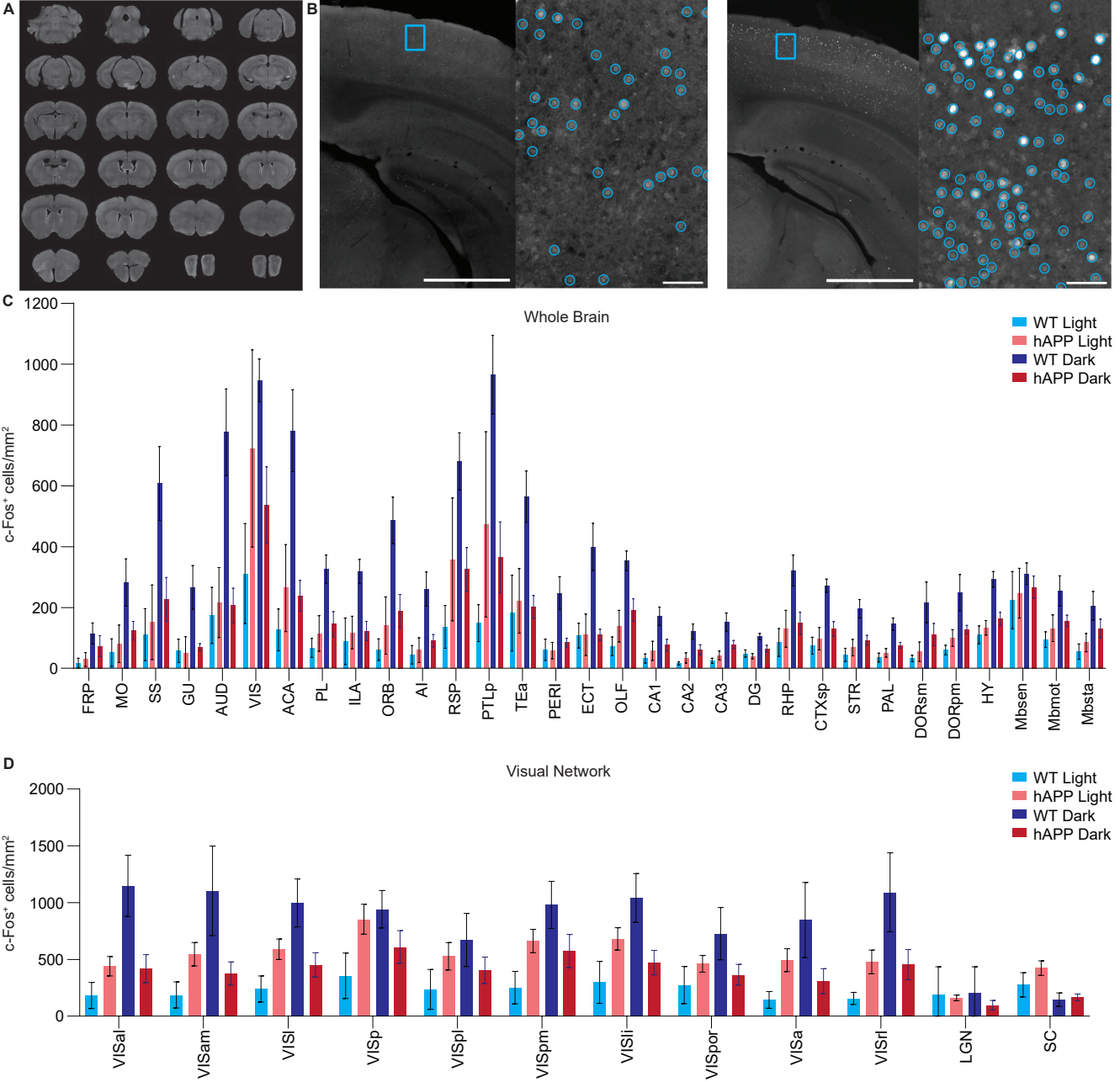
A
B
C
Whole Brain
WT Light
hAPP Light
WT Dark
hAPP Dark
c-Fos+ cells/mm2
1200
1000
800
600
400
200
0
FRP
MO
SS
GU
AUD
VIS
ACA
PL
ILA
ORB
AI
RSP
PTLp
TEa
PERI
ECT
OLF
CA1
CA2
CA3
DG
RHP
CTXsp
STR
PAL
DORsm
DORpm
HY
Mbsen
Mbmot
Mbsta
D
Visual Network
WT Light
hAPP Light
WT Dark
hAPP Dark
c-Fos+ cells/mm2
2000
1500
1000
500
0
VISal
VISam
VISl
VISp
VISpl
VISpm
VISli
VISpor
VISa
VISrl
LGN
SC

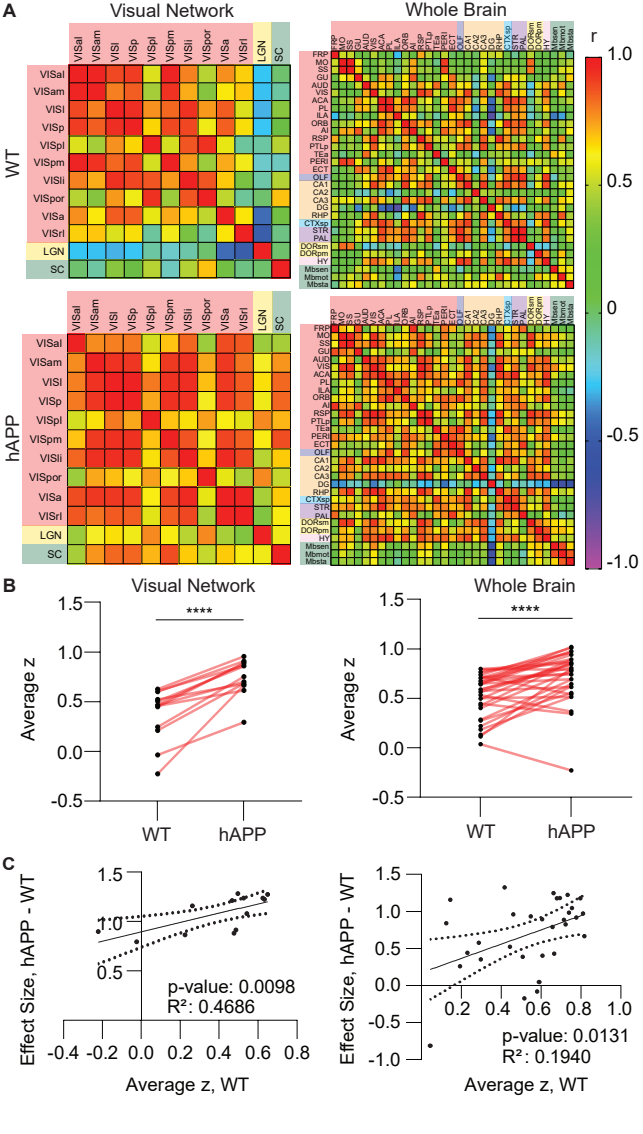
A
Visual Network
Whole Brain
WT
hAPP
VISal
VISam
VISl
VISp
VISpl
VISpm
VISli
VISpor
VISa
VISrl
LGN
SC
r
1.0
0.5
0
-0.5
-1.0
B
Visual Network
Whole Brain
Average z
****
WT
hAPP
C
Effect Size, hAPP - WT
Average z, WT
p-value: 0.0098
R²: 0.4686
p-value: 0.0131
R²: 0.1940

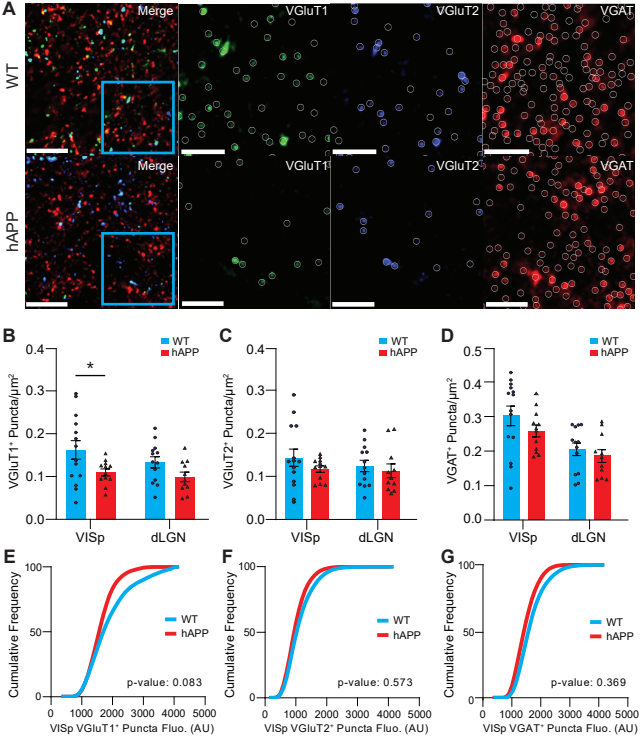
A
WT
hAPP
Merge
VGluT1
VGluT2
VGAT
B
C
D
WT
hAPP
VGluT1+ Puncta/μm2
VGluT2+ Puncta/μm2
VGAT+ Puncta/μm2
*
VISp
dLGN
E
F
G
Cumulative Frequency
p-value: 0.083
p-value: 0.573
p-value: 0.369
VISp VGluT1+ Puncta Fluo. (AU)
VISp VGluT2+ Puncta Fluo. (AU)
VISp VGAT+ Puncta Fluo. (AU)

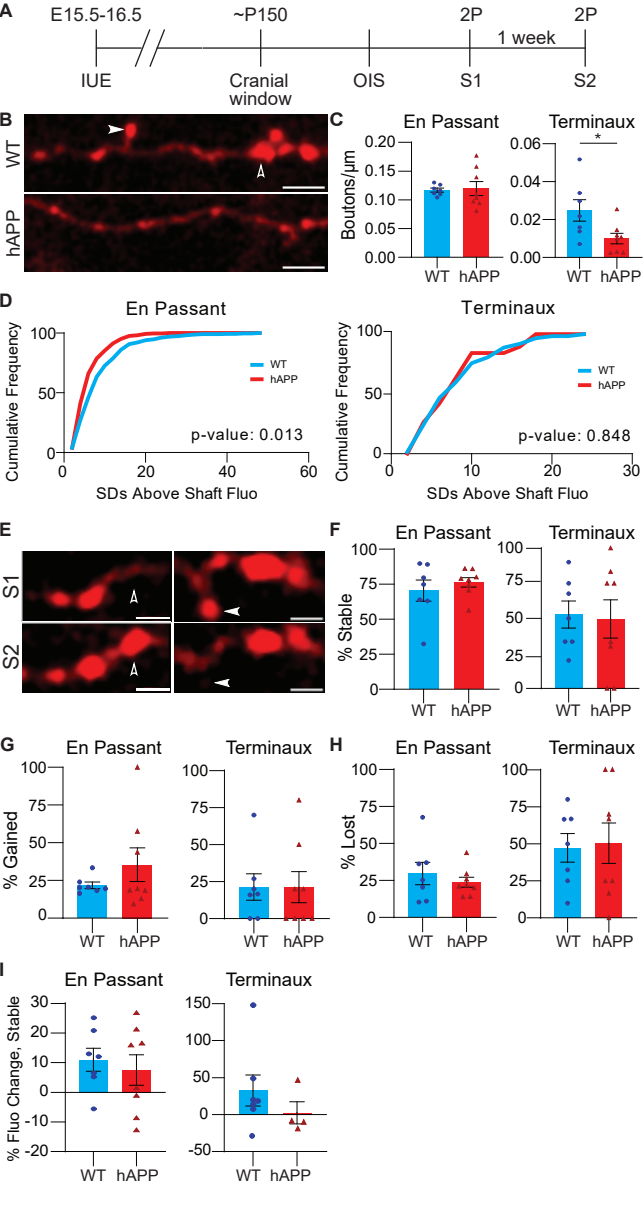
A
E15.5-16.5
~P150
2P
2P
1 week
IUE
Cranial window
OIS
S1
S2
B
WT
hAPP
C
En Passant
Terminaux
Boutons/µm
0.20
0.15
0.10
0.05
0.00
0.06
0.04
0.02
0.00
*
WT
hAPP
D
En Passant
Terminaux
Cumulative Frequency
100
50
0
WT
hAPP
p-value: 0.013
p-value: 0.848
0
20
40
60
10
20
30
SDs Above Shaft Fluo
E
S1
S2
F
En Passant
Terminaux
% Stable
100
75
50
25
0
WT
hAPP
G
En Passant
Terminaux
% Gained
H
En Passant
Terminaux
% Lost
I
En Passant
Terminaux
% Fluo Change, Stable
30
20
10
0
-10
-20
150
100
50
0
-50

	WT L vs. hAPP L	WT D vs. hAPP D	WT L vs. WT D	hAPP L vs. hAPP D
FRP	-	-	-	-
MO	-	-	-	-
SS	-	-	*	-
GU	-	-	-	-
AUD	-	*	*	-
VIS	*	-	****	-
ACA	-	*	*	-
PL	-	-	**	-
ILA	-	*	**	-
ORB	-	*	**	-
AI	-	-	*	-
RSP	*	-	**	-
PTLp	-	*	**	-
TEa	-	*	*	-
PERI	-	-	*	-
ECT	-	*	*	-
OLF	*	*	***	-
CA1	-	-	*	-
CA2	-	-	*	-
CA3	*	-	*	-
DG	-	-	**	-

RHP	-	-	*	-
CTXsp	-	**	***	-
STR	-	-	**	-
PAL	-	-	**	-
DORsm	-	-	-	-
DORpm	-	-	*	-
HY	-	*	***	-
Mbsen	-	-	-	-
Mbmot	-	-	-	-
Mbsta	-	-	-	-

Table 1: **Whole brain mixed-effects ANOVA of c-Fos$^+$ cell density, WT and hAPP mice, light and dark conditions.** Selected comparisons of c-Fos$^+$ cell density. n = 8 WT light, 7 WT dark, 9 hAPP light, and 6 hAPP dark housed mice, mixed-effects ANOVA with Tukey's multiple comparisons test. Brain region effect (within subject)****, experimental condition effect (between subjects)****, interaction****. *p-value < 0.05, **p-value < 0.01, ***p-value < 0.001, ****p-value < 0.0001.

	WT L vs. hAPP L	WT D vs. hAPP D	WT L vs. WT D	hAPP L vs. hAPP D
VISal	-	**	***	-
VISam	*	*	**	-
VISl	*	*	****	-
VISp	*	-	***	-
VISpl	-	-	**	-
VISpm	*	-	****	-
VISli	*	**	****	-
VISpor	-	-	**	-
VISa	*	*	**	-
VISrl	-	*	**	-
LGN	-	-	-	-
SC	-	-	-	*

Table 2: **Visual Network mixed-effects ANOVA c-Fos$^+$ cell density, WT and hAPP mice, light and dark conditions.** Selected comparisons of c-Fos$^+$ cell density. n = 8 WT light, 7 WT dark, 9 hAPP light, and 6 hAPP dark housed mice, mixed-effects ANOVA with Tukey's multiple comparison tests. Brain region effect (within subject)****, experimental condition effect (between subjects)****, interaction****. *p-value < 0.05, **p-value < 0.01, ***p-value < 0.001, ****p-value < 0.0001.